Modulating excitonic recombination effects through one-step synthesis of perovskite nanoparticles for light-emitting diodes

Kulkarni, Sneha Avinash; Muduli, Subas; Xing, Guichuan; Yantara, Natalia; Li, Mingjie; Chen, Shi; Sum, Tze Chien; Mathews, Nripan; White, Tim J; Mhaisalkar, Subodh Gautam

2017

Kulkarni, S. A., Muduli, S., Xing, G., Yantara, N., Li, M., Chen, S., . . . Mhaisalkar, S. G. (2017). Modulating excitonic recombination effects through one-step synthesis of perovskite nanoparticles for light-emitting diodes. ChemSusChem, 10(19), 3818-3824. doi:10.1002/cssc.201701067

https://hdl.handle.net/10356/140976

https://doi.org/10.1002/cssc.201701067

Modulating Excitonic Recombination Effects through One-Step Synthesis of Perovskite Nanoparticles for Light-Emitting Diodes

Sneha A. Kulkarni,[a] Subas Muduli,[a] Guichuan Xing,[b] Natalia Yantara,[a] Mingjie Li,[c] Shi Chen,[c] Tze Chien Sum,[c] Nripan Mathews,*[a, d] Tim J. White,[d] and Subodh G. Mhaisalkar*[a, d]

The primary advantages of halide perovskites for light-emitting diodes (LEDs) are solution processability, direct band gap, good charge-carrier diffusion lengths, low trap density, and reasonable carrier mobility. The luminescence in 3D halide perovskite thin films originates from free electron-hole bimolecular recombination. However, the slow bimolecular recombination rate is a fundamental performance limitation. Perovskite nanoparticles could result in improved performance but processability and cumbersome synthetic procedures remain challenges. Herein, these constraints are overcome by tailoring the 3D perovskite as a near monodisperse nanoparticle film prepared through a one-step in situ deposition method. Replacing methyl ammonium bromide (CH_3NH_3Br, MABr) partially by octyl ammonium bromide [$CH_3(CH_2)_7NH_3Br$, OABr] in defined mole ratios in the perovskite precursor proved crucial for the nanoparticle formation. Films consisting of the in situ formed nanoparticles displayed signatures associated with excitonic recombination, rather than that of bimolecular recombination associated with 3D perovskites. This transition was accompanied by enhanced photoluminescence quantum yield (PLQY & 20.5 % vs. 3.40 %). Perovskite LEDs fabricated from the nanoparticle films exhibit a one order of magnitude improvement in current efficiency and doubling in luminance efficiency. The material processing systematics derived from this study provides the means to control perovskite morphologies through the selection and mixing of appropriate additives.

Introduction

Organic–inorganic hybrid perovskites show promise as low-cost materials in high performance optoelectronics[1–5] with power conversion efficiencies in solar cells reaching 22.1 %[1–6] and ongoing advances in light-emitting diodes (LEDs), lasing, and photodetector applications.[4,7–13] These halide perovskites can be prepared easily through solution processing and possess excellent tunable optical properties across the visible range.[7,14–17] Metal-halide perovskite chemical analogues are alternatives to organic molecules for solution-processed LED applications and efficiencies of 8.8 % with tunable emission have been realized.[18–22] However, the slow free electron-hole bimolecular radiative recombination required for efficient photovoltaic operation limits LED performance.[21] Consequently, the external quantum efficiency (EQE) of the LEDs is limited by defect-state trapping (a first order decay process) rather than bimolecular radiative recombination (a second order decay process). The electrical injected charge-carrier density is typically $< 10^{16}$ cm^{-3} and is comparable to 3D perovskite trap densities. One approach to achieve high luminescence quantum yield (QY) at reasonable carrier densities ($n \leq 10^{15}$ cm^{-3}) and moderate trap-state density is to replace the second order bimolecular recombination with first order excitonic recombination. At injected carrier density below 10^{16} cm^{-3}, a nearly invariant luminescence QY as high as 90% could be achieved if we can tailor the luminescence from excitonic recombination with a decay rate of 10^8 s^{-1} (trap-assisted monomolecular recombination coefficient $= 10^7$ s^{-1}, Auger recombination coefficients $= 10^{-26}$ cm^6 s^{-1}, Figure S1]. This transition from free-carrier bimo-

[a] Dr. S. A. Kulkarni, Dr. S. Muduli, Dr. N. Yantara, Prof. N. Mathews, Prof. S. G. Mhaisalkar
Energy Research Institute at Nanyang Technological University (ERI@N)
Research Techno Plaza, X-Frontier Bloc Level 5
50 Nanyang Drive, Singapore 637553 (Singapore)
E-mail: Nripan@ntu.edu.sg
Subodh@ntu.edu.sg

[b] Prof. G. Xing
Institute of Applied Physics and Materials Engineering
University of Macau
Avenida da Universidade, Taipa, Macau (P. R. China)

[c] Dr. M. Li, Dr. S. Chen, Prof. T. C. Sum
Division of Physics and Applied Physics
School of Physical and Mathematical Sciences
Nanyang Technological University
21 Nanyang Link, Singapore 637371 (Singapore)

[d] Prof. N. Mathews, Prof. T. J. White, Prof. S. G. Mhaisalkar
School of Materials Science and Engineering
Nanyang Technological University
Nanyang Avenue, Singapore, 639798 (Singapore)

lecular recombination to excitonic recombination can be enabled through the utilization of perovskite nanoparticles (NPs). In perovskite nanocrystals, excitonic emission competes effectively with the charge-carrier trapping process to achieve much higher photoluminescence quantum yields (PLQY) than from bulk perovskite films. However, structurally uniform and chemically pure nanocrystal films with physical integrity are difficult to fabricate. Moreover, ligand binding to perovskite nanocrystal surfaces in commonly used solvents is highly dynamic, and can dissociate during isolation and purification leading to nanocrystal aggregation.[23–25] This further restricts solution processing of subsequent device layers. Commonly used long-chain organic capping/stabilizing ligands such as oleic acid and oleylamine can suppress charge injection, limit brightness, and result in high turn-on voltage in LED devices.[29–31] Thus, it is challenging to form a compact and ligand-free film from preformed nanoparticles. A more elegant approach would be to induce the in situ/one-step formation of perovskite nanocrystals during the film formation process.

Here, we describe the formation of $MAPbBr_3$ perovskite NP films directly during the film formation process, by completely eschewing ligands such as oleylamine and oleic acid. This was enabled by the utilization of octyl ammonium bromide [$CH_3(CH_2)_7NH_3Br$, OABr] as a partial substituent for methyl ammonium bromide (CH_3NH_3Br, MABr) in the precursor. The role of OABr is to regulate crystal growth rate. The precursor solutions were prepared in ratios of MABr/OABr ranging from 1:0 (0%), 0.98:0.02 (2%), 0.95:0.05 (5%), 0.90:0.10 (10%), and 0.80 :0.20 (20 %), while maintaining the overall mole ratio of MABr + OABr/$PbBr_2$ at 1:1. The film morphology was characterized by electron microscopy whereas the photophysical properties were evaluated to obtain the functional signatures of the nanoparticulate film.

Results and Discussion

Solution-processed perovskite bulk crystal films were directly tailored into near monodisperse nanocrystal films on substrate surfaces through a one-step in situ deposition (Figures 1 and 2), which avoided the restrictions associated with preformed NP solutions. In this method, the precursor solution was spin-coated at 6000 rpm for 12 s, followed by dripping toluene (150 μL) for 10 s into the spinning process (Figures 1a and S2).[26] Subsequently, the film was annealed at 100 ^{0}C for 5 min. The perovskite NP films formed by partial substitution of 10 mol % of OABr for MABr in the perovskite precursor (Figure 1 b) were homogenous. No color change of the perovskite precursor solution was evident after OABr addition. Standard $MAPbBr_3$ perovskite films prepared under the same experimental conditions consist of large crystallites ranging from approximately 0.5 to 2 μm (Figure 1 c), demonstrating that OABr addition invariably leads to a significant reduction in crystallite size (Figure 1 d–f). For instance, the film formed with a MABr/OABr = 0.98 :0.02 mole ratio (2 % OABr, Figure 1 d), exhibits smaller crystallites (< 100 nm) than standard $MAPbBr_3$. However, along with the small crystallites, randomly distributed large crystals (> 2 μm) also appear (Figure S3). The addition of

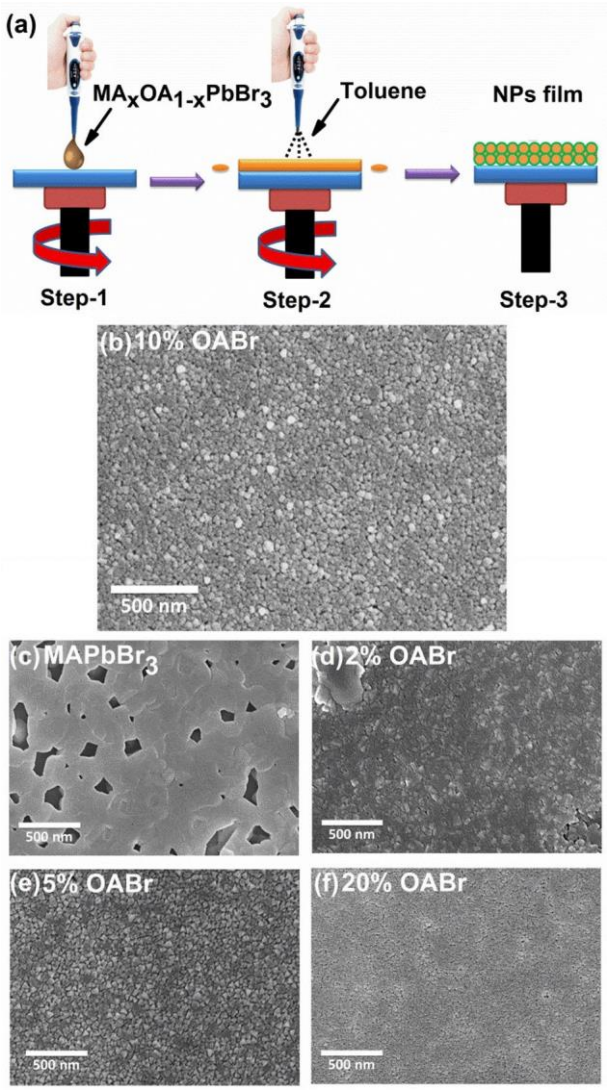

Figure 1. (a) One-step in situ deposition method of perovskite NP film formation. Step 1: perovskite precursor solution preparation using mixed cation approach using OABr and MABr in defined mole ratios in DMF with spin-coating speed 6000 rpm for 12 s; Step 2: toluene (150 *m*L) dispensed after 10 s during spinning; Step 3: uniform perovskite NP film. FESEM images of films using: b) 10% OABr (0.90 :0.10); c) standard $MAPbBr_3$ (0 % OABr) ; d) 2% OABr (0.98:0.02); e) 5 % OABr (0.95 :0.05); f) 20% OABr (0.80:0.20).

2 mol% OABr was insufficient to form uniform films. Increasing OABr to 5% yields about 37 nm cuboidal crystals (calculated from powder X-ray diffraction, XRD, vide infra) (Figure 1 e). Compact film formation was maintained with increasing OABr up to 20 mol% (Figure 1 f). A dense perovskite film with particle size of 22 nm (calculated from XRD, vide infra) was formed from 10 mol % OABr addition. Cross-section and transmission electron diffraction (TED) mode field-emission scanning electron microscopy (FESEM) further reveals larger perovskite crystals in the case of standard $MAPbBr_3$, whereas 10 % OABr promotes NP formation (Figure S4). XRD was used to examine the crystallinity as a function of MABr/OABr content using the characteristic strong reflection at $2\theta = 14.8^0$ (for CuK_a radiation) corresponding to the (100) reflection of cubic perovskite (Fig-

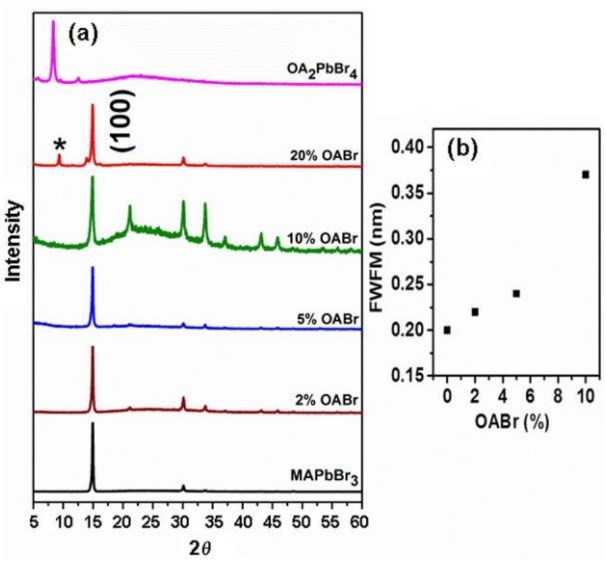

Figure 2. (a) Superimposed XRD patterns of perovskite films; 2 θ in the range 5–60⁰ along with reference pure 2D perovskite of $(OA)_2PbBr_4$ (* peak due to quasi 2D perovskite); (b) FWHM for (100) peak.

ure 2 a).[27] The full-width half maximum (FWHM) broadened from 0.20 to 0.22, 0.23, and 0.37δ 2q as the mole ratio of MABr to OABr increases from 1:0 to 0.98:0.02, 0.95:0.05, and 0.90 :010, indicative of the decrease by volume of crystal domains (Figure 2 b). An extra peak at 2 θ= 9.4⁰ appears in the film prepared with 20 % OABr, typical of quasi 2D perovskite formation.[15]

Comparison with the diffraction patterns of OA_2PbBr_4 indicated that phase separation had not occurred in the OABr substituted films. A broadening of the (100) reflection for the film prepared using 10 % OABr is consistent with a reduction in grain size observed by FESEM. In the $MAPbX_3$ perovskite crystal structure, methyl ammonium cations are located in the cavity created by corner-sharing $[PbX_6]^{4-}$ octahedra (simple cubic cell, $Pm\bar{3}m$), but the octyl ammonium bromide cations adsorb on the outer surface, which prohibits further crystal growth.[28] A composition of 10 mol% OABr with respect to MABr proved optimal to form spherical nanoparticles, but higher additions favor 2D perovskite.[28] NP formation by utilizing shorter alkane chain bromides such as ethyl ammonium bromide ($CH_3CH_2NH_3Br$, EABr) and butyl ammonium bromide ($CH_3CH_2CH_2NH_3Br$, BuABr) were also attempted. Films formed at similar compositions, that is, MABr:EABr and MABr/BuABr in 0.90 :0.10 mole ratio resulted in smaller perovskite crystallites. However, their columnar nature and larger dimensions may attenuate excitonic behavior and further optimization is required (Figure S5). NP film formation for different methyl ammonium lead-halide precursors was also investigated. Accordingly, compact and nanocrystalline perovskite films were fabricated with $MAPbI_3$, $MAPbI_{1.5}Br_{1.5}$, $MAPbBr_{0.5}Cl_{0.5}$, and $MAPbCl_3$ with partial substitution of corresponding octyl ammonium halide salts (i.e., OAI, OABr, and OACl) in their respective perovskite precursor solutions. The optical absorption, PL and electroluminescence (EL) spectra are shown in Figures S6 and S7. The success of OABr as an additive to promote facile, repeatable perovskite nanoparticle formation motivated us to examine the system further utilizing $MAPbBr_3$ NPs as focus.

For TEM measurements, the film was separated from the glass surface, dispersed in toluene, and the suspension mounted on a holey carbon grid (Figure 3 a, b). The average nanoparticle size is around 15 nm (inset of Figure 3 a) with a lattice spacing of 0.29 nm corresponding to the (002) planes of $MAPbBr_3$ perovskite (Figure 3 c). The selected-area electron diffraction (SAED) pattern is made up of discrete spots as expected for nanocrystalline $MAPbBr_3$ perovskite (Figure 3 d).[29] Optical absorption measurements showed an absorption onset for all films at 540 nm, corresponding to a band gap of approximately 2.30 eV, typical of $MAPbBr_3$.The additional peak at 450 nm for the 20 % OABr film arises from the quasi 2D perovskite (Figure 3 e).

The superimposed PL spectra of $MAPbBr_3$ (0 % OABr) and nanoparticle perovskite films (10 % OABr) show no shift in the PL peak position, $\lambda = 534$ nm, but its intensity is enhanced by almost two orders of magnitude (inset of Figure 4 a). The 10 % OABr nanoparticle perovskite film exhibits a noticeably higher PLQY of 20.5 %, compared to the standard perovskite film with PLQY of 3.40 %, signifying higher radiative recombination. The perovskite films show that the 10 % OABr NP film is visibly brighter than the standard film under UV illumination (Hg lamp, 365 nm) (Figure 4 a). There is a systematic enhancement in PL intensity and green fluorescence with OABr addition, possibly owed to surface passivation and carrier confinement effects (Figure S8). The PL decay curves were fitted using a biex- ponential decay function to extract lifetimes and amplitude weighted average lifetimes. The fast and slow time constants were attributed, respectively to the recombination of excitons in the defect rich regions (i.e., dominated by the non-radiative recombination near nanoparticle surfaces) and the defect-free regions (i.e., dominated by the radiative component inside the NPs) (Figure S9). The average PL lifetime in the standard sample was ι=4.3 ns whereas the 10 % OABr $MAPbBr_3$ perov- skite film yields ι=6.9 ns (Table S1). This longer PL lifetime of 10 % OABr perovskite NP film is attributed to the reduced non-radiative recombination with fewer surface trap states, arising from surface passivation, as well as the carrier confinement effect of OABr. The motivation behind the pursuit of perovskite NPs is to exploit the excitonic nature of their emission processes to form high performance LEDs. To confirm the excitonic nature of the emission, further photophysical characterization was performed. Figure 4b summarizes the initial time PL intensity [$I_{PL}(t = 0)$] as a function of the injected carrier density for both the perovskite nanocrystals film (10 % OABr) and normal 3D perovskite ($MAPbBr_3$) film. Under low fluence pumping, $I_{PL}(t = 0)$ gives a clear signature of the quadratic power dependence of the recombination rate on the carrier densities, confirming the bimolecular type recombination in the normal 3 D perovskite film. On the other hand, for the perovskite nanocrystals film, $I_{PL}(t = 0)$ is almost linearly ($y \propto x^{1.4}$) dependent on the injected carrier density from 2 x 10^{15} to 5 x 10^{17} cm^{-3} (Figure 4 b). This result suggests that a large portion of the luminescence in the perovskite nanocrystals film originates from

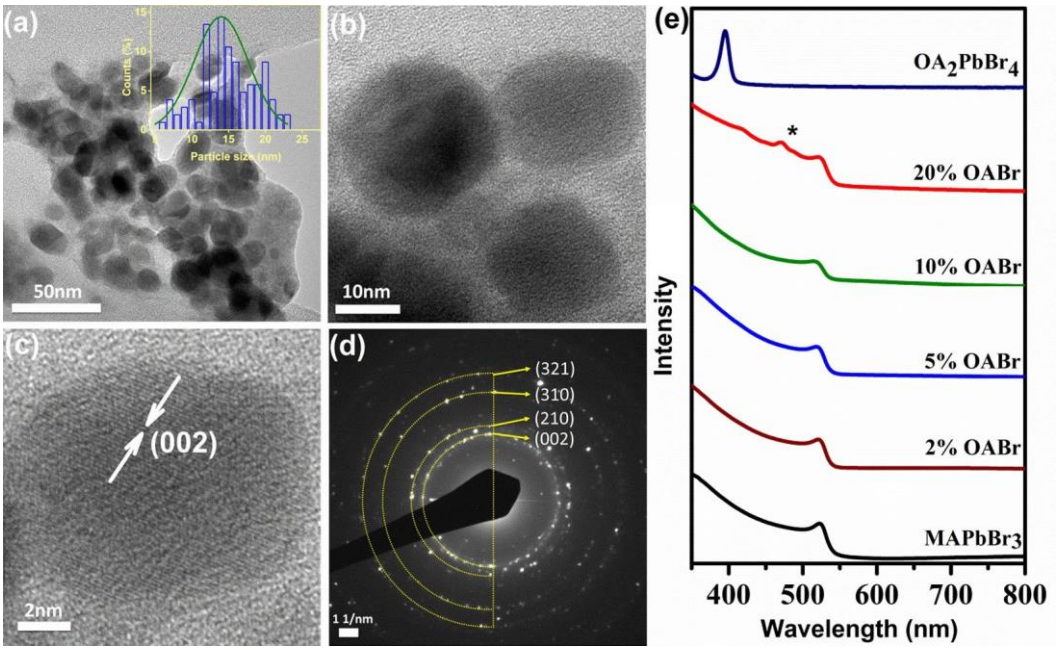

Figure 3. TEM images of $MAPbBr_3$ NPs film prepared using 10 % OABr addition (a, b), inset of (a) shows size distribution histogram of perovskite nanoparticles; (c) HRTEM images of nanoparticles; (d) SAED pattern of $MAPbBr_3$ nanoparticles; (e) superimposed UV/Vis spectra of films prepared using in situ single-step deposition method by varying the mole ratio of MABr/OABr in $MAPbBr_3$ perovskite precursors (2 %, 5%, 10%, and 20 % OABr), and for reference, the $(OA)_2PbBr_4$ spectrum (* indicates absorption due to quasi 2D perovskite formation).

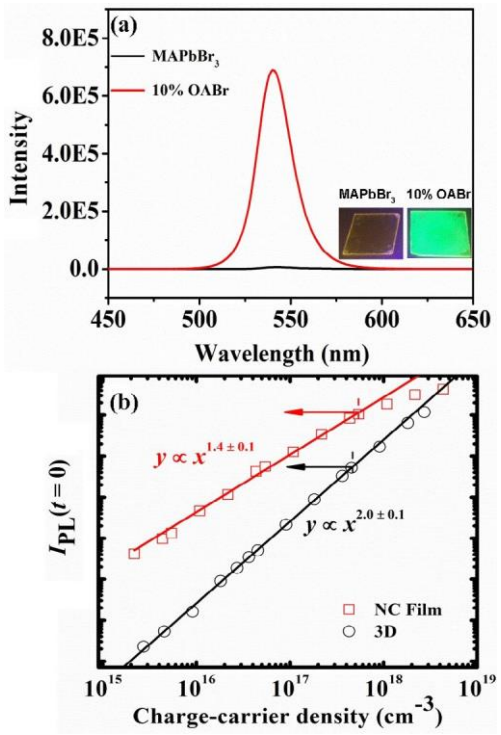

Figure 4. (a) Superimposed PL spectra of standard (0 % OABr) and nanoparticle (10 % OABr) perovskite films (excitation wavelength= 400 nm), showing the latter with about two orders of magnitude higher PL under UV illumination (Hg lamp, 365 nm); these films were prepared under identical experimental conditions in the inert atmosphere. (b) Confirmation of the excitonic recombination-dominated decay in the perovskite nanocrystals film. Photon-injected charge-carrier density dependence of the initial time PL intensity [$I_{PL}(t = 0)$] following excitation at 400 nm (1 KHz, 100 fs).

first-order excitonic emission. However, owing to the size distribution, some large nanocrystals in the film may still exhibit behavior like 3D perovskites (charge carrier decay through free electron-hole bimolecular recombination). Overall, these findings demonstrate that excitonic recombination-dominated decay could be achieved by tailoring the perovskite as nanocrystal films through a simple one-step in situ deposition method. Hence, better device performance is expected when the LED is constructed using the perovskite NP film. Accordingly, LEDs were fabricated using standard (0 % OABr) and 10 % OABr $MAPbBr_3$ NP perovskites as the emissive layer. For the device fabrication, the $MAPbBr_3$ and nanoparticles on PEDOT:PSS [poly(2,3-dihydrothieno-1,4-dioxin)-poly(styrenesulfonate)] were coated on an indium-doped tin oxide (ITO) substrate (Figure 5 a). The bathophenanthroline (BPhen) electron transport layer (ETL) together with the electrode consisting of Ca and Ag were prepared by thermal evaporation. UV photoelectron spectra (UPS) measurements of the 10 % OABr perovskite showed no measurable shift in band-gap energy of $MAPbBr_3$ (Figure S10). The energy levels of Bphen and the Ca/Ag electrode were taken from the literature.[30,31] The preliminary perovskite LED characteristics are summarized in Figure 5 c–e. Ohmic conduction behaviour ($J = V$) was observed on the J–V curves up to 1.4 and 1.6 V for the 0% OABr and 10 % OABr device, respectively. Comparable ohmic or leakage currents were observed in both devices. At higher voltages, the current increases exponentially as a function of voltage, indicating a trap-limited conduction regime ($J \approx V^m$ with $m = 1$ for ohmic conduction, $m = 2$ for space-charge-limited current, and $m > 2$ for trap-limited conduction).

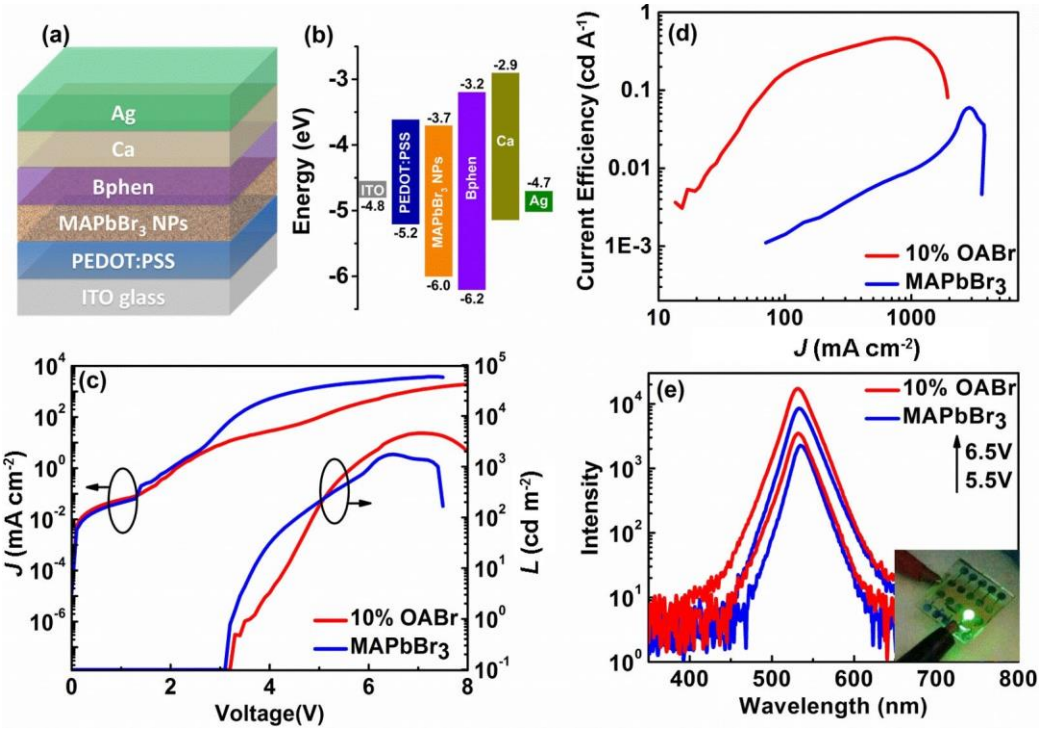

Figure 5. (a) Schematic representation of the perovskite LED device structure for standard $MAPbBr_3$ (0 %) and nanoparticle (10 % OABr) films along with (b) the energy levels diagram;[30,31] corresponding (c) current density and luminance curve versus characteristics voltage, (d) current efficiency (cd A^{-1}) versus current density, (e) EL spectra of the devices at different current density (mA $cm^{@2}$). Inset shows photograph of nanoparticle perovskite-based LED working device.

A gentler slope (less steep) was observed in 10 % OABr devices in the trap-limited conduction regime, indicating slower charge transport caused by the existence of multiple grain boundaries in the carrier-transport path. A space-charge-limited current regime ($J \approx V^2$) was observed above 4 and 7.2 V for the 0% OABr and 10 % OABr device, respectively (Fig- ure S11). Higher turn-on voltage (V_{th}) for the onset of lumi- nance (V_{th} defined as luminance at 1 cd m^{-2}) is observed for the perovskite LED device with 10 % OABr (3.6 V) compared to the device with 0% OABr (3.2 V). This could be attributed to the slower charge transport into the emitter with 10 % OABr, in agreement with the reduction in slope of the *J–V* curves. A higher luminescence maximum (L_{max}) is recorded for the device with 10 % OABr content (L_{max} = 4578 cdm^{-2}) than the 0% OABr PeLED device (L_{max} = 1754 cdm^{-2}). The current efficiency of 10 % OABr perovskite LED device is an order of magnitude higher than the pure $MAPbBr_3$ device attributed to higher radiative recombination in the 10 % OABr perovskite film (higher PLQY = 20.5 %). Despite poorer charge transport, the use of 10 % OABr enhances the radiative recombination through carrier confinement in the NPs, which leads to better device efficiency. The EL spectra of both devices peaked at 530 nm in agreement with the PL spectra and independent of external bias (Figure 5e). During the preparation of this work, several approaches of in situ perovskite NP film formation have been demonstrated.[32–34] These include in situ $MAPbBr_3$ nanocrystalline thin film formation using excess of MABr in the $MAPbBr_3$ precursor solution[32] and the addition of excess butyl ammonium bromide (BABr) in $MAPbBr_3$ precursor to obtain perovskite thin films with small crystallites. Although the current efficiency of the standard $MAPbBr_3$ device was poor (0.06 cd A^{-1}), the improved performance (15 cd A^{-1}) was reported after nanocrystalite film formation.[33] Herein, we report improved PLQY (20.5 %) for nanocrystalline film compared to standard $MAPbBr_3$ thin films (3.4 %), which demonstrates clear improvement in the emissive properties of the perovskite thin film. However, the EQE of the LED devices based on perovskite NPs film is lower,[33] which may be due to the imbalance between electron and hole injection to the emitter. MA/OA would generate different sets of conduction and valence band energy levels compared to those of the earlier reported BABr system.[33] Thus, varying the hole-injection layer or electron-injection layer that matches OABr would further boost the EQE of the resulting LED device based on the perovskite NPs film prepared using OABr addition. In brief, improved device performance could be attained with modified device architecture, optimal perovskite layer thickness, as well as controlled device fabrication conditions under inert atmosphere.

Conclusions

Excitonic recombination-dominated decay processes were demonstrated by tailoring perovskite nanocrystalline films through a one-step in situ deposition method. This was achieved by systematic replacement of OABr (octyl ammonium bromide) for MABr (methyl ammonium bromide) in defined

mole ratios in the perovskite precursor. The OABr addition does not disturb the crystal structure or optical properties of the perovskite, but controls particle growth to form a nanocrystal film. Moreover, the photoluminescence quantum yield (PLQY = 20.5 %), lifetime (t ≈6.9 ns), and device performance (L_{max} = 4578 cdm^{-2}, 0.6 cd A^{-1}) of the modified perovskite were enhanced compared to standard the $MAPbBr_3$ perovskite film. This was attributed to surface passivation and carrier confinement effects. This method overcomes the limitations of film fabrication for device applications from preformed precursor solution, and through further tuning of the additive composition and concentration, superior devices with optimal nanocrystal morphologies can be fabricated.

Experimental Section

Device fabrication: the perovskite-based LED devices were fabricated on ITO-coated (7 *W* cm^{-}) glass substrates. The substrates were cleaned by successive bath sonication in decon soap, distilled water, and finally ethanol. The samples were then dried under N_2 and treated in oxygen plasma for 20 min. A film of PEDOT:PSS (Clevios PVP Al 4083) was spin-coated on a clean substrate at 4000 rpm for 60 s and annealed at 130 8C for 15 min in air to remove water from the PSS shell of the PEDOT:PSS grains. The standard $MAPbBr_3$ perovskite solution was prepared by mixing equimolar amounts of MABr (Aldrich, 99.9 %) and $PbBr_2$ (Aldrich, + 98 %) in dimethyl formamide (DMF) solvent. Similarly, the perovskite solutions with OABr (Aldrich, 99.9 %) addition were prepared by varying the mole ratio of MABr/OABr viz. 1:0 (0%), 0.98:0.02 (2 %), 0.95 :0.05 (5 %), 0.90:0.10 (10 %), 0.80:0.20 (20 %) while maintaining the final precursor mole ratio of MABr + OABr/PbBr2 at 1:1. The solutions were stirred for 10–12 h at room temperature and subsequently filtered with a 0.250 *m*m PVDF (polyvinylidene difluoride) filter before spin-coating in a glovebox at 6000/5000 rpm for 12 s to form a thin-film on the PEDOT:PSS-coated ITO substrate. The toluene was dispensed after 10 s during dynamic spin coating. The perovskites were annealed at 1008C for 5 min. For reference, the, octyl ammonium lead bromide [$(OA)_2PbBr_4$] perovskite precursor solution was prepared by mixing OABr and $PbBr_2$ in a 2:1 mole ratio in DMF. Similarly, perovskite solutions were also prepared using EABr and BABr, that is, mixing MABr/EABr and MABr/BABr in a 0.90:0.10 mole ratio along with 1 mol of $PbBr_2$ in DMF. This was followed by evaporation of a 30 nm Bphen layer, then Ca (5 nm), and Ag (100 nm) as electron-transport layers at a base pressure of 1 V 10^{-5} torr (1 torr = 133.322 Pa) to complete the process of device fabrication. The devices were encapsulated inside the glovebox and testing conducted at ambient conditions.

Device characterization: The characteristic current density–voltage (*J*–*V*) curves of the perovskite LED devices were recorded with an Agilent B2902 instrument. A precision source/measure unit and luminous output of the devices was measured by a LS-110 Konica Minolta luminance meter. All of these instruments were connected to a computer and operated through LabVIEW software.

The spectral response of EL emission was collected by a Shimadzu RF-5301pc spectrofluorophotometer after blocking the excitation beam. The absolute PLQYs were recorded using an Ocean-optics USB4000 spectrometer with an integrated sphere excited at a wavelength of 400 nm.

Time-resolved PL measurements: TRPL data were collected using an Optronis Optoscope streak camera system with an ultimate temporal resolution of around 10 ps. The laser source was a Coherent Libra regenerative amplifier (50 fs, 1 KHz, 800 nm) seeded by a Coherent Vitesse oscillator (50 fs, 80 MHz). The 400 nm pump pulses were obtained by frequency doubling the 800 nm fundamental regenerative amplifier output with a BBO crystal.

Optical absorption spectroscopy: The absorbance spectra of these perovskite films were recorded using UV/Vis-NIR spectrophotometer (UV-3600 Shimadzu) equipped with integrating sphere.

FESEM: FESEM imaging was performed using a JEOL JSM-7600F scanning electron microscope at 5–10 kV with a working distance of & 8 mm. The samples (standard $MAPbBr_3$ and NP perovskite) for FESEM TED mode analysis were prepared removing/scratching films from the substrate, dispersing in toluene, and drop casting on holey carbon grids.

High-resolution TEM: HRTEM imaging was performed using a TEM JEOL 2010 HR instrument at an accelerating voltage of 200 keV. The perovskite NP film was removed/scratched from the substrate, dispersed in toluene, and subsequently a drop of solvent drop cast on holey carbon grids.

XRD: XRD measurements were performed with Bruker D8 Advance X-ray diffractometer using Ni-filtered CuK_a radiation.

Acknowledgements

Authors would like to thank Dr. Ajay Perumal and Mr. Yan Fong Ng for their valuable help in LED device fabrication and PLQY measurements, respectively. S.A.K acknowledges the financial support from Johnson Matthey PLC, UK. G.X. thanks the support from the Science and Technology Development Fund from Macau SAR (FDCT-116/2016/A3) and Start-up Research Grant (SRG2016-00087-FST) from Research & Development Office at University of Macau. T.C.S. acknowledges the financial support Ministry of Education Academic Research Fund Tier 1 grants M4011530 and M4011769, and Tier 2 grants MOE2014-T2-1-044, MOE2015-T2-2-015 and MOE2016-T2-1-034. Funding from the Singapore National Research Foundation through the Singapore-Berkeley Research Initiative for Sustainable Energy (SinBeRISE) CREATE Program and the Competitive Research Program NRF-CRP14-2014-03 is acknowledged.

Conflict of interest

The authors declare no conflict of interest.

Keywords: exciton formation · light emitting diodes · methyl ammonium lead bromide · nanoparticles · perovskites

[1] A. Kojima, K. Teshima, Y. Shirai, T. Miyasaka, *J. Am. Chem. Soc.* 2009, *131*, 6050.

[2] M. M. Lee, J. Teuscher, T. Miyasaka, T. N. Murakami, H. J. Snaith, *Science* 2012, *338*, 643.

[3] M. Saliba, T. Matsui, J.-Y. Seo, K. Domanski, J.-P. Correa-Baena, M. K. Nazeeruddin, S. M. Zakeeruddin, W. Tress, A. Abate, A. Hagfeldt, M. Gr-tzel, *Energy Environ. Sci.* 2016, *9*, 1989.

[4] G. Xing, N. Mathews, S. S. Lim, N. Yantara, X. Liu, D. Sabba, M. Gr-tzel, S. Mhaisalkar, T. C. Sum, *Nat. Mater.* 2014, *13*, 476.

[5] G. Xing, N. Mathews, S. Sun, S. S. Lim, Y. M. Lam, M. Gr-tzel, S. Mhaisalkar, T. C. Sum, *Science* 2013, *342*, 344.
[6] S. A. Kulkarni, T. Baikie, P. P. Boix, N. Yantara, N. Mathews, S. Mhaisalkar, *J. Mater. Chem. A* 2014, *2*, 9221.
[7] A. Sadhanala, S. Ahmad, B. Zhao, N. Giesbrecht, P. M. Pearce, F. Deschler, R. L. Hoye, K. C. Godel, T. Bein, P. Docampo, S. E. Dutton, M. F. De Volder, R. H. Friend, *Nano Lett.* 2015, *15*, 6095.
[8] Z.-K. Tan, R. S. Moghaddam, M. L. Lai, P. Docampo, R. Higler, F. Deschler, M. Price, A. Sadhanala, L. M. Pazos, D. Credgington, F. Hanusch, T. Bein, H. J. Snaith, R. H. Friend, *Nat. Nanotechnol.* 2014, *9*, 687.
[9] S. Colella, M. Mazzeo, A. Rizzo, G. Gigli, A. Listorti, *J. Phys. Chem. Lett.* 2016, *7*, 4322.
[10] L. Dou, Y. Yang, J. You, Z. Hong, W.-H. Chang, G. Li, Y. Yang, *Nat. Commun.* 2014, *5*, 5404.
[11] S. A. Veldhuis, P. P. Boix, N. Yantara, M. Li, T. C. Sum, N. Mathews, S. G. Mhaisalkar, *Adv. Mater.* 2016, *28*, 6804.
[12] C. C. Stoumpos, C. D. Malliakas, M. G. Kanatzidis, *Inorg. Chem.* 2013, *52*, 9019.
[13] Y.-H. Kim, C. Wolf, H. Cho, S.-H. Jeong, T.-W. Lee, *Adv. Mater.* 2016, *28*, 734.
[14] S. Pathak, N. Sakai, F. Wisnivesky Rocca Rivarola, S. D. Stranks, J. Liu, G. E. Eperon, C. Ducati, K. Wojciechowski, J. T. Griffiths, A. A. Haghighirad, A. Pellaroque, R. H. Friend, H. J. Snaith, *Chem. Mater.* 2015, *27*, 8066.
[15] S. Bhaumik, S. A. Veldhuis, Y. F. Ng, M. Li, S. K. Muduli, T. C. Sum, B. Damodaran, S. Mhaisalkar, N. Mathews, *Chem. Commun.* 2016, *52*, 7118.
[16] M. I. Saidaminov, J. Almutlaq, S. Sarmah, I. Dursun, A. A. Zhumekenov, R. Begum, J. Pan, N. Cho, O. F. Mohammed, O. M. Bakr, *ACS Energy Lett.* 2016, *1*, 840.
[17] F. Zhang, C. Chen, S. V. Kershaw, C. Xiao, J. Han, B. Zou, X. Wu, S. Chang, Y. Dong, A. L. Rogach, H. Zhong, *ChemNanoMat* 2017, *3*, 303.
[18] J. Wang, N. Wang, Y. Jin, J. Si, Z.-K. Tan, H. Du, L. Cheng, X. Dai, S. Bai, H. He, Z. Ye, M. L. Lai, R. H. Friend, W. Huang, *Adv. Mater.* 2015, *27*, 2311.
[19] H. Cho, S.-H. Jeong, M.-H. Park, Y.-H. Kim, C. Wolf, C.-L. Lee, J. H. Heo, A. Sadhanala, N. Myoung, S. Yoo, S. H. Im, R. H. Friend, T.-W. Lee, *Science* 2015, *350*, 1222.
[20] J. Byun, H. Cho, C. Wolf, M. Jang, A. Sadhanala, R. H. Friend, H. Yang, T.-W. Lee, *Adv. Mater.* 2016, *28*, 7515.
[21] M. Yuan, L. N. Quan, R. Comin, G. Walters, R. Sabatini, O. Voznyy, S. Hoogland, Y. Zhao, E. M. Beauregard, P. Kanjanaboos, Z. Lu, D. H. Kim, E. H. Sargent, *Nat. Nanotechnol.* 2016, *11*, 872.
[22] C. Wehrenfennig, G. E. Eperon, M. B. Johnston, H. J. Snaith, L. M. Herz, *Adv. Mater.* 2014, *26*, 1584.
[23] Y. Kim, E. Yassitepe, O. Voznyy, R. Comin, G. Walters, X. Gong, P. Kanjanaboos, A. F. Nogueira, E. H. Sargent, *ACS Appl. Mater. Interfaces* 2015, *7*, 25007.
[24] J. De Roo, M. Ib#Çez, P. Geiregat, G. Nedelcu, W. Walravens, J. Maes, J. C. Martins, I. Van Driessche, M. V. Kovalenko, Z. Hens, *ACS Nano* 2016, *10*, 2071.
[25] T. A. Berhe, W.-N. Su, C.-H. Chen, C.-J. Pan, J.-H. Cheng, H.-M. Chen, M.-C. Tsai, L.-Y. Chen, A. A. Dubale, B.-J. Hwang, *Energy Environ. Sci.* 2016, *9*, 323.
[26] K. Kara, D. A. Kara, C. Kırbıyık, M. Ersoz, O. Usluer, A. L. Briseno, M. Kus, *RSC Adv.* 2016, *6*, 26606.
[27] P. Schulz, E. Edri, S. Kirmayer, G. Hodes, D. Cahen, A. Kahn, *Energy Environ. Sci.* 2014, *7*, 1377.
[28] S. Aharon, L. Etgar, *Nano Lett.* 2016, *16*, 3230.
[29] Q. Zhu, K. Zheng, M. Abdellah, A. Generalov, D. Haase, S. Carlson, Y. Niu, J. Heimdal, A. Engdahl, M. E. Messing, T. Pullerits, S. E. Canton, *Phys. Chem. Chem. Phys.* 2016, *18*, 14933.
[30] J.-A. Yoon, Y.-H. Kim, N. H. Kim, S. I. Yoo, S. Y. Lee, F. R. Zhu, W. Y. Kim, *Nanoscale Res. Lett.* 2014, *9*, 191.
[31] C.-C. Chueh, C.-Z. Li, A. K. Y. Jen, *Energy Environ. Sci.* 2015, *8*, 1160.
[32] J.-W. Lee, Y. J. Choi, J.-M. Yang, S. Ham, S. K. Jeon, J. Y. Lee, Y.-H. Song, E. K. Ji, D.-H. Yoon, S. Seo, H. Shin, G. S. Han, H. S. Jung, D. Kim, N.-G. Park, *ACS Nano* 2017, *11*, 3311.
[33] Z. Xiao, R. A. Kerner, L. Zhao, N. L. Tran, K. M. Lee, T.-W. Koh, G. D. Scholes, B. P. Rand, *Nat. Photonics* 2017, *11*, 108.
[34] H. P. Kim, J. Kim, B. S. Kim, H.-M. Kim, J. Kim, A. R. b. M. Yusoff, J. Jang, M. K. Nazeeruddin, *Adv. Opt. Mater.* 2017, *5*, 1600920.